4308 *Biochemistry* **2010,** *49,* 4308–4317
DOI: 10.1021/bi1002585

BIOCHEMISTRY
including biophysical chemistry & molecular biology
Article

Mutation of Asn28 Disrupts the Dimerization and Enzymatic Activity of SARS 3CL^{pro}†,‡

Jennifer Barrila,§ Sandra B. Gabelli,‖ Usman Bacha,§ L. Mario Amzel,‖ and Ernesto Freire*,§

§*Department of Biology, Johns Hopkins University, Baltimore, Maryland 21218, and*
‖*Department of Biophysics and Biophysical Chemistry, Johns Hopkins University School of Medicine, Baltimore, Maryland 21205*

Received February 19, 2010; Revised Manuscript Received April 20, 2010

ABSTRACT: Coronaviruses are responsible for a significant proportion of annual respiratory and enteric infections in humans and other mammals. The most prominent of these viruses is the severe acute respiratory syndrome coronavirus (SARS-CoV) which causes acute respiratory and gastrointestinal infection in humans. The coronavirus main protease, 3CL^{pro}, is a key target for broad-spectrum antiviral development because of its critical role in viral maturation and high degree of structural conservation among coronaviruses. Dimerization is an indispensable requirement for the function of SARS 3CL^{pro} and is regulated through mechanisms involving both direct and long-range interactions in the enzyme. While many of the binding interactions at the dimerization interface have been extensively studied, those that are important for long-range control are not well-understood. Characterization of these dimerization mechanisms is important for the structure-based design of new treatments targeting coronavirus-based infections. Here we report that Asn28, a residue 11 Å from the closest residue in the opposing monomer, is essential for the enzymatic activity and dimerization of SARS 3CL^{pro}. Mutation of this residue to alanine almost completely inactivates the enzyme and results in a 19.2-fold decrease in the dimerization K_d. The crystallographic structure of the N28A mutant determined at 2.35 Å resolution reveals the critical role of Asn28 in maintaining the structural integrity of the active site and in orienting key residues involved in binding at the dimer interface and substrate catalysis. These findings provide deeper insight into complex mechanisms regulating the activity and dimerization of SARS 3CL^{pro}.

Coronaviruses are prevalent human and veterinary pathogens that are associated with a variety of respiratory and enteric diseases. In recent years, a number of novel coronaviruses have been discovered, including the severe acute respiratory syndrome coronavirus (SARS-CoV),[1] which causes a dangerous atypical pneumonia in humans (*1*−*6*). The lack of effective anti-coronavirals emphasizes the urgent need for broad-spectrum inhibitors against these viruses in preparation for future outbreaks of highly virulent strains. Success in the design of a broad-spectrum inhibitor depends on the identification and characterization of a target that is essential for the viral life cycle and is highly conserved among all coronaviruses. The main viral protease, SARS 3CL^{pro}, shares a high degree of structural conservation with other coronavirus 3CL proteases and plays a critical role in viral replication through the processing of two large polyproteins to produce a mature viral replicase complex (*7*, *8*). The functional importance of 3CL^{pro} in the viral life cycle and its high degree of structural conservation have made it one of the most promising targets for broad-spectrum coronavirus inhibitor development.

Structural studies performed with SARS 3CL^{pro} have demonstrated that the enzyme is a 68 kDa homodimer in solution (*9*−*28*). Each 34 kDa protomer is comprised of three structural domains and possesses an intact active site cavity formed by the first two domains of the protein. The catalytic residues lie within a chymotrypsin-like double-β-barrel fold comprised of the first two domains of the protein (residues 1−184). These catalytic domains are connected by a long loop region (residues 185−200) to a third globular domain composed of five antiparallel α-helices (residues 201−306). The efficiency with which the enzyme is able to perform substrate catalysis is closely linked with its ability to dimerize (*9*−*28*). Extensive mutational analyses of residues located at the dimerization interface of SARS 3CL^{pro} have led to the identification of key interactions between the N-terminus of one protomer and the second and third domains of the opposing protomer that are critical for mediating dimer formation (*9*−*28*). Lai and coworkers demonstrated that complete disruption of the dimer interface with peptides derived from the N-terminus of the protein results in the inactivation of the protease, supporting the idea that the development of dimerization inhibitors is a promising drug design approach for this target (*9*, *12*).

We previously reported that dimerization is not controlled only through direct contacts at the dimer interface but also coordinated through long-range interactions (*21*). Specifically, it was determined that serine 147, a highly conserved residue located more than 9 Å from the closest residue in the opposing monomer, is critical for maintaining the proper enzymatic

†Supported by National Institutes of Health Grant GM57144.
‡Atomic coordinates and structure factors have been deposited in the Protein Data Bank as entry 3FZD.
*To whom correspondence should be addressed: Department of Biology, Johns Hopkins University, 3400 N. Charles St., Baltimore, MD 21218. Phone: (410) 516-7743. Fax: (410) 516-6469. E-mail: ef@jhu.edu.
[1]Abbreviations: SARS, severe acute respiratory syndrome; SARS-CoV, severe acute respiratory syndrome coronavirus; 3CL^{pro}, 3C-like protease; SDS−PAGE, sodium dodecyl sulfate−polyacrylamide gel electrophoresis; DSC, differential scanning calorimetry; IPTG, isopropyl β-D-thiogalactopyranoside; TCEP, tris(2-carboxyethyl)phosphine hydrochloride; EDTA, ethylenediaminetetraacetic acid; EK, enterokinase; PDB, Protein Data Bank.

 Published on Web 04/26/2010 © 2010 American Chemical Society

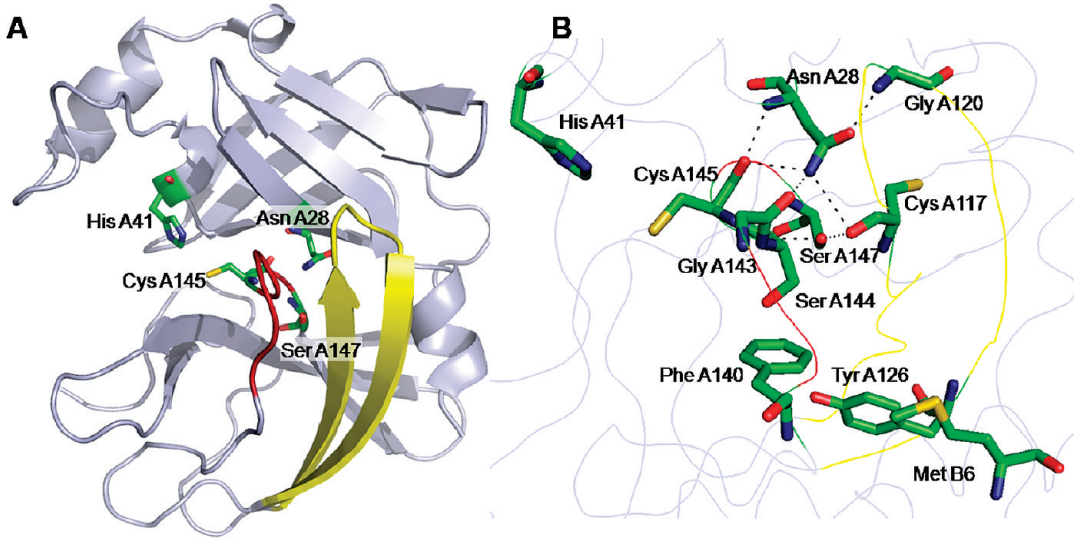

C

```
                          ....|....|  ....|....|  ....|....|  ....|....|
                               5          15         25         35
SARS HCoV TOR2            SGFRKMAFPS GKVEGCMVQV TCGTTTLNGL WLDDTVYCPR
HCoV HKU1                 SGIVKMVSPT SKIEPCIVSV TYGSMTLNGL WLDDKVYCPR
HCoV NL63                 SGLKKMAQPS GCVERCVVRV CYGSTVLNGV WLGDTVTCPR
HCoV OC43                 SGIVKMVNPT SKVEPCVVSV TYGNMTLNGL WLDDKVYCPR
HCoV 229E                 AGLRKMAQPS GFVEKCVVRV CYGNTVLNGL WLGDIVYCPR
SARS Civet007             SGFRKMAFPS GKVEGCMVQV TCGTTTLNGL WLDDTVYCPR
Bat CoV HKU9-2            AGLTRMAHPS GLVEPCVVKV SYGSMTLNGV WLDNFVMCPR
TGEV Miller M6            SGLRKMAQPS GLVEPCIVRV SYGNNVLNGL WLGDEVICPR
PEDV                      AGLRKMAQPS GVVEKCIVRV CYGNMALNGL WLGDIVMCPR
MHV A59                   SGIVKMVSPT SKVEPCIVSV TYGNMTLNGL WLDDKVYCPR
Bovine Alpaca             SGIVKMVNPT SKVEPCIVSV TYGNMTLNGL WLDDKVYCPR
Giraffe US/OH3-TC/20      SGIVKMVNPT SKVEPCIVSV TYGNMTLNGL WLDDKVYCPR
IBV                       SGFKKLVSPS SAVEKCIVSV SYRGNNLNGL WLGDTIYCPR
FIPV                      SGLRKMAQPS GVVEPCIVRV AYGNNVLNGL WLGDEVICPR
```

FIGURE 1: Location of Asn28 within the catalytic domains of wild-type SARS 3CL^{pro}. (A) SARS 3CL^{pro} catalytic domains (residues 8−184) [PDB entry 2BX4 (*18*)] are depicted in ribbon representation. The loop containing residues 140−147 is colored red and the β-sheet containing residues 111−128 yellow. Residues Asn28, His41, Cys145, and Ser147 are shown as sticks and colored by atom type, with carbons colored green, nitrogens blue, oxygens red, and sulfurs yellow. (B) Key residues surrounding Asn28 are depicted as sticks and colored by atom type as in panel A. Hydrogen bonding interactions made by Asn28 and Ser147 were calculated using Chimera (*47*) and are represented by black dotted lines. (C) Asn28 is highly conserved among coronavirus 3CL proteases. The sequence alignment of 14 coronavirus 3CL proteases was produced using ClustalW (*48*). The first 40 residues are shown. Asn28 is highlighted in yellow in each of the sequences. GenBank accession numbers for protein sequences are as follows: SARS-CoV (Tor2 strain), AAP41036; HCoV HKU1 (genotype A), AY597011; HCoV NL63, AY567487; HCoV OC43, AY903460; HCoV 229E, AF304460; SARS civet (palm civet isolate 007), AAU04645; bat CoV (strain HKU9-2), AAZ41328; TGEV (Miller M6 strain), ABG89299; PEDV, NP_598309; MHV A59 (A59 strain), NP_045298; BCV alpaca (alpaca strain), ABI93997; giraffe CoV (strain US/OH3-TC/2006); IBV, AAY24431; FIPV, ABI14447.

activity and dimerization of SARS 3CL^{pro} (*21*). Mutation of this residue to alanine completely interfered with the dimerization and activity of the protease. In the wild-type structure, the side chain hydroxyl of Ser147 donates two hydrogen bonds to the backbone carbonyls of Ser144 and Cys117, as shown in Figure 1. These interactions are part of an intricate hydrogen bonding network surrounding the active site of the protein. We postulated that the interactions formed by the side chain of Ser147 are instrumental in maintaining the position of the critical loop defined by residues 139−147 with respect to the adjacent β-sheet, which contains residues Cys117 and Tyr126. Although the structural basis for this dramatic effect was not readily apparent on the basis of the location of Ser147 within the structure of the wild-type enzyme, two possible mechanisms were proposed. In the first mechanism, loss of the interaction between Ser147 and Ser144 may induce a repositioning of Phe140 which would disrupt the hydrophobic pocket formed by Phe140 and Tyr126 from the same chain and Met6 from the opposing chain. Met6 was previously shown to be important for the activity and dimerization of the protease (*9*). In the second mechanism, the loss of the hydrogen bonding interaction between the side chain of Ser147 and the backbone of Cys117 may result in the repositioning of the β-sheet on which Cys117 resides. This change will affect Tyr126 (located on the opposite end of the β-sheet containing Cys117), thereby disrupting its aromatic stacking interaction with Phe140 of the same chain and the hydrophobic interaction with Met6 from the opposing chain. Alternatively, a combination of these two possibilities may also explain the diminished capacity of the S147A mutant to dimerize.

On the basis of the key interactions made by the side chain of Ser147 in wild-type coronavirus, we hypothesized that Asn28, another highly conserved residue adjacent to the active site cavity, but ~11 Å from the closest residue in the opposing monomer, may also be important in preserving enzymatic activity and dimerization of SARS 3CL^{pro} (*21*). Asn28 is a buried residue that makes extensive interactions with both the catalytic loop and the β-sheet where Cys117 is located (Figure 1B), suggesting that this residue, like Ser147, may also play a central role in regulating the dimerization and activity of the protease. If so, disrupting the key interactions made by the side chain of Asn28 would likely result in severe losses in enzymatic activity and dimerization, despite the fact that Asn28 is not located at

the dimerization interface. While Asn28 itself does not lie in a cavity that can be targeted with small molecule inhibitors, the elucidation of the network of interactions that control the dimerization and activity of $3CL^{pro}$ provides new avenues for the development of novel allosteric inhibitors of the enzyme.

In this study, we determined that the interactions formed by Asn28 are indeed important for maintaining both the enzymatic activity and dimerization of SARS $3CL^{pro}$. Mutation of this residue to alanine rendered the enzyme almost completely inactive and resulted in a 19.2-fold decrease in the dimerization K_d. To elucidate the structural basis for the observed loss of activity and dimerization, a crystallographic structure of the N28A mutant was determined at 2.35 Å resolution. The N28A structure revealed that the mutation induced significant rearrangements in and around the active site of the enzyme as compared to previously determined wild-type SARS $3CL^{pro}$ structures. Specifically, the side chains of residues Cys145 and Cys117 flipped almost 180° from their locations in the wild type to form a novel disulfide bond in the structure of the N28A mutant. While a majority of the interactions at the dimer interface remained intact as compared to those of the wild-type protease, no electron density was observed for residues Ser139, Phe140, and Leu141, indicating that these residues are most likely disordered in the N28A structure. The disorder observed for these particular residues is significant given the recent finding that residues Ser139, Phe140, and Leu141 may be involved in an overlapping network linking catalysis and dimerization in the enzyme (*27*). The results presented here confirm that long-range interactions in SARS $3CL^{pro}$ are critical for maintaining its oligomeric state and activity and provide additional evidence that dimerization and catalysis are linked through key residues that collectively regulate enzymatic function.

EXPERIMENTAL PROCEDURES

Cloning. cDNA encoding full-length SARS $3CL^{pro}$ (Tor2 strain, GenBank entry AY274119) was previously cloned into a pET 100 vector (Champion pET Directional TOPO Expression and Cloning Kit, Invitrogen) which carries an N-terminal polyhistidine tag, an enterokinase cleavage site for removal of the affinity tag, and ampicillin resistance (*29*). The N28A mutation was introduced using an in vitro site-directed mutagenesis kit (QuickChange, Stratagene) with the pET-SARS $3CL^{pro}$ vector as the template. The sequences of the primers used to generate the N28A mutant were 5′ GGA ACT ACA ACT CTT GCT GGA TTG TGG TTG G 3′ and the reverse complement. Following the polymerase chain reaction (PCR) conducted with Pfu turbo DNA polymerase (Stratagene), the parent template was degraded with a DpnI (Stratagene) digestion reaction for 1 h at 37 °C. One-shot TOPO10 competent cells (Invitrogen) were transformed with the PCR product for plasmid amplification. The plasmid was then purified, and the mutations were confirmed by DNA sequencing.

Protein Expression and Purification. Recombinant wild-type and N28A SARS $3CL^{pro}$ were expressed as a soluble fraction in BL21 Star DE3 *Escherichia coli* competent cells (Invitrogen) and purified as previously described (*21*, *29*). Cells were grown in LB supplemented with ampicillin (50 μg/mL) at 37 °C, induced with 1 mM IPTG when the absorbance at 600 nm was between 0.8 and 1.0, and harvested after 4 h. Cells were resuspended in lysis buffer [50 mM potassium phosphate (pH 7.8), 400 mM sodium chloride, 100 mM potassium chloride, 10% glycerol, 0.5% Triton-X, and 10 mM imidazole]. The cells were broken by sonication on ice for short pulses of 1 s followed by 3 s off for a total of 16 min. The cell debris was collected by centrifugation (20000*g* at 4 °C for 45 min). The supernatant was filtered using a 0.45 μm pore size filter (Millipore) and applied directly to a nickel affinity column (HiTrap Chelating HP, Amersham Biosciences) that had been pre-equilibrated with binding buffer [50 mM sodium phosphate, 0.3 M sodium chloride, and 10 mM imidazole (pH 8.0)]. The protease was eluted with a linear gradient of 50 mM sodium phosphate, 0.3 M sodium chloride, and 250 mM imidazole (pH 8.0). After elution, the protein buffer was exchanged into a buffer containing 10 mM Tris-HCl (pH 7.5) and loaded onto a Q-Sepharose anion exchange column (Amersham Biosciences). The protease was eluted with a gradient of a buffer consisting of 10 mM Tris-HCl and 1 M NaCl (pH 7.5). The buffer of the pooled fractions containing $3CL^{pro}$ was exchanged into 10 mM sodium phosphate, 10 mM NaCl, 1 mM TCEP, and 1 mM EDTA (pH 7.4) and digested for 48 h at 4 °C with enterokinase (Invitrogen, 0.1 unit per 112 μg of protease) to remove the N-terminal polyhistidine tag. The enterokinase was removed by incubation with EK-away resin according to the manufacturer's instructions (Invitrogen). The reaction mixture was passed through a nickel affinity column to remove undigested protease. The digested protein was run over a HiLoad 16/60 Superdex 75 column (Amersham Biosciences) equilibrated with 10 mM Tris-HCl, 0.1 M NaCl, 1 mM EDTA, and 1 mM TCEP (pH 7.4). Protease-containing fractions were concentrated to 10 mg/mL. Samples were more than 95% pure, as assessed by SDS−PAGE.

Kinetics. The catalytic activities of wild-type and N28A SARS $3CL^{pro}$ were determined as previously described (*16*, *21*) using a fluorescence-based peptide cleavage assay with a commercially available fluorogenic substrate, Dabcyl-KTSAVLQS-GFRKME-Edans (Genesis Biotech), which corresponds to the N-terminal autocleavage site of the protease. The change in fluorescence intensity was monitored in a Cary Eclipse fluorescence spectrophotometer (Varian) with 355 and 538 nm excitation and emission wavelengths, respectively. The experiments were performed in 10 mM sodium phosphate, 10 mM sodium chloride, 1 mM EDTA, and 1 mM TCEP (pH 7.4). Kinetic parameters such as K_m and k_{cat} were determined by initial rate measurement of substrate cleavage at 25 °C. The reaction was initiated by the addition of substrate such that the final concentration varied from 1 to 80 μM.

Differential Scanning Calorimetry. The heat capacities of wild-type $3CL^{pro}$ and the N28A mutant were measured as a function of temperature with a high-precision differential scanning VP-DSC microcalorimeter (Microcal Inc., Northampton, MA). The experiments were performed in 10 mM sodium phosphate, 10 mM sodium chloride, 1 mM EDTA, and 1 mM TCEP (pH 7.4). Protein samples and reference solutions were properly degassed and carefully loaded into the cells to avoid bubble formation. Thermal denaturation scans were performed with freshly prepared buffer-exchanged protease solutions using a temperature scan rate of 1 °C/min. Data were analyzed with software developed in this laboratory.

Analytical Ultracentrifugation. Sedimentation velocity and equilibrium experiments were conducted using a Beckman-Coulter XL-I analytical ultracentrifuge. Wild-type and N28A samples were prepared by being loaded onto a HiLoad 16/60 Superdex 75 column (Amersham Biosciences) into 10 mM Tris-HCl, 0.1 M NaCl, 1 mM TCEP, and 1 mM EDTA (pH 7.4). For sedimentation velocity experiments, reference (420 μL) and sample (400 μL) solutions were loaded into double-sector centerpieces and mounted in a Beckman An60Ti rotor. Experiments

were performed at 20 °C and 0.5 mg/mL with a rotor speed of 50000 rpm. Sample absorbance at 280 nm was monitored in a continuous mode with no delay and a step size of 0.003 cm without averaging. Multiple scans at different time points were fit to a continuous size distribution using SEDFIT version 9.3b (*30*). The $c(s)$ distribution in SEDFIT was exported to SEDPHAT where experimental values were corrected to $S_{20,w}$ (*31*). A partial specific volume of 0.7310 cm^3/g for wild-type $3CL^{pro}$ or 0.7314 cm^3/g for the N28A mutant was used in all calculations based on the amino acid sequence of the protein. The solvent density and viscosity were calculated using SEDNTERP (J. Philo, http://www.jphilo.mailway.com/default.htm). Sedimentation equilibrium experiments were performed in the same buffer as sedimentation velocity experiments at 0.25, 0.5, and 1 mg/mL (7.4, 14.8, and 29.5 μM, respectively). Reference (120 μL) and sample (110 μL) solutions were loaded into six-sector centerpieces and mounted in a Beckman An60Ti rotor. Samples were equilibrated at 20 °C and three speeds: 15000, 20000, and 25000 rpm. The sample absorbance at 280 or 250 nm was collected in step mode with a step size of 0.001 cm and 10 replicates at each radial position. WinMatch (Biotechnology-Bioservices Center, University of Connecticut, Storrs, CT) was used to determine when samples reached equilibrium. Equilibrium was attained for all samples between 24 and 30 h. All samples were visually inspected for clarity to ensure no precipitation had occurred during the runs. Dissociation constants were determined by global fitting of multiple concentrations and rotor speeds in SEDPHAT using the monomer−dimer equilibrium model (*32*).

Crystallization, Structure Determination, and Refinement. To obtain crystals of the SARS $3CL^{pro}$ N28A mutant, a condition used to crystallize wild-type SARS $3CL^{pro}$ was used as a starting condition (*13*). The best crystals grew in hanging drop experiments with a 500 μL reservoir solution containing 1.0 M sodium malonate (pH 7.0) and 5−6% 2-propanol. The drop was made using 2 μL of reservoir solution and 2 μL of protein solution [6 mg/mL protein in 10 mM Tris-HCl (pH 7.4), 0.1 M NaCl, 1 mM EDTA, and 1 mM TCEP]. Crystals grew within 1−3 days at room temperature as clusters which were then separated into single crystals for diffraction.

The structure of N28A SARS $3CL^{pro}$ was determined by molecular replacement with AMoRe (*33*) using wild-type SARS $3CL^{pro}$ as a search model [PDB entry 2BX4 (*18*)]. Crystals belonged to space group $P2_12_12$ with the following cell dimensions: a = 105.9 Å, b = 44.8 Å, and c = 54.2 Å. One protease monomer was present per asymmetric unit. The dimer was generated through 2-fold crystallographic symmetry. For the final crystal structure refinement, data were collected from a crystal flash-frozen using 20% glycerol as the cryoprotectant at beamline X6A at the National Synchrotron Light Source, Brookhaven National Laboratory (Upton, NY). The final model was refined to 2.35 Å resolution with an R value of 21.7% (R_{free} = 27.7%). Intensity data were integrated, scaled, and reduced to structure factor amplitudes with the HKL2000 suite (*34*), as summarized in Table 1. Restrained refinement of the models was performed using REFMAC (*35*). Manual building was conducted using O (*36*), and water molecules were placed with Arp-WARP (*37*). The stereochemistry of the model was checked and analyzed using PROCHECK and MolProbity (*38*). The coordinates for the structure of N28A SARS $3CL^{pro}$ have been deposited in the Protein Data Bank (entry 3FZD).

Table 1: Data Collection and Refinement Statistics for N28A SARS $3CL^{pro}$

Data Collection	
space group	$P2_12_12$
cell dimensions a, b, c (Å)	105.9, 44.8, 54.2
resolution (Å)	50.00−2.35 (2.43−2.35)[a]
R_{sym}	0.073 (0.578)[a]
I/σ	22.7 (1.9)[a]
completeness (%)	99.9 (99.6)[a]
redundancy	5.3 (4.4)[a]
X-ray source	X6A
wavelength (Å)	0.9537
Refinement	
resolution (Å)	50.0−2.35
no. of reflections	10705
R_{work}/R_{free}	0.217/0.277 (0.276/0.307)[a]
no. of atoms	
protein	2322
water	99
B factor (Å^2)	
protein	34.19
water	46.34
rmsd[b]	
bond lengths (Å)	0.009
bond angles (deg)	1.1

[a]Parentheses indicate values for the highest-resolution shell. [b]Root-mean-square deviation.

RESULTS AND DISCUSSION

Asn28 is absolutely conserved in $3CL^{pro}$ amino acid sequences derived from various coronavirus species (Figure 1C), suggesting that it plays an essential role in the activity of this enzyme. In existing crystallographic structures, Asn28 is 11 Å from the closest residue in the opposing monomer. However, the side chain of Asn28 makes a number of key interactions with residues within and surrounding the active site of SARS $3CL^{pro}$, as shown in Figure 1A,B. To investigate the importance of this residue in maintaining the enzymatic activity and oligomeric state of SARS $3CL^{pro}$, we mutated Asn28 to alanine and expressed, purified, and analyzed the recombinant protein in the same manner that was used for the wild-type enzyme.

The N28A Mutation Drastically Reduces the Enzymatic Activity of SARS $3CL^{pro}$. The enzymatic activity of the N28A mutant was characterized using a fluorescence-based cleavage assay to determine the Michaelis constant (K_m) and the catalytic rate constant (k_{cat}) as previously described (*21*, *29*, *39*). The results of the cleavage assay are shown in Figure 2A and summarized in Table 2. The N28A mutant had a K_m of 67.83 ± 6.62 μM, which is comparable to the value of 56.42 ± 9.18 μM we previously determined for the wild-type enzyme with the same substrate (*21*), suggesting that the mutation did not interfere with the ability of the enzyme to bind the substrate. However, a large decrease in the value of k_{cat} was observed relative to that of the wild-type enzyme. The k_{cat} for N28A was 0.012 ± 0.001 s^{-1}, which is a 54-fold decrease relative to the wild-type value of 0.643 ± 0.051 s^{-1}. This value is, however, higher than the k_{cat} observed for the monomeric S147A mutant which was 0.004 ± 0.001 s^{-1} (*21*).

The N28A Mutant Is Folded. Thermal denaturation of the N28A mutant was performed using differential scanning calorimetry to examine the effect of the mutation on the stability of the protein. Figure 2B shows the temperature dependence of the heat capacity function of wild-type $3CL^{pro}$ versus the N28A

mutant in 10 mM sodium phosphate, 10 mM NaCl, 1 mM EDTA, and 1 mM TCEP (pH 7.4). The denaturation transition for wild-type 3CL^{pro} is centered at 56.50 ± 0.1 °C at a protein concentration of 0.2 mg/mL (5.9 μM) and temperature scanning rate of 1 °C/min. Like those of the wild-type protease, the N28A calorimetric scans were irreversible due to precipitation, so a full thermodynamic analysis could not be performed. The N28A mutation had an effect on the denaturation transition for the protease similar to that of the previously reported S147A mutation (*21*). A downward shift in T_m of 1.8 °C was observed compared to that of the wild-type enzyme (the S147A mutant displayed a downward shift of 1.7 °C), as summarized in Table 2. The area under the curve, ΔH, was similar to that of the wild type, indicating that there were no major structural rearrangements that occurred due to the mutation. These results confirmed that the N28A mutant is folded and indicate that the mutation did not significantly affect the overall stability of the protein.

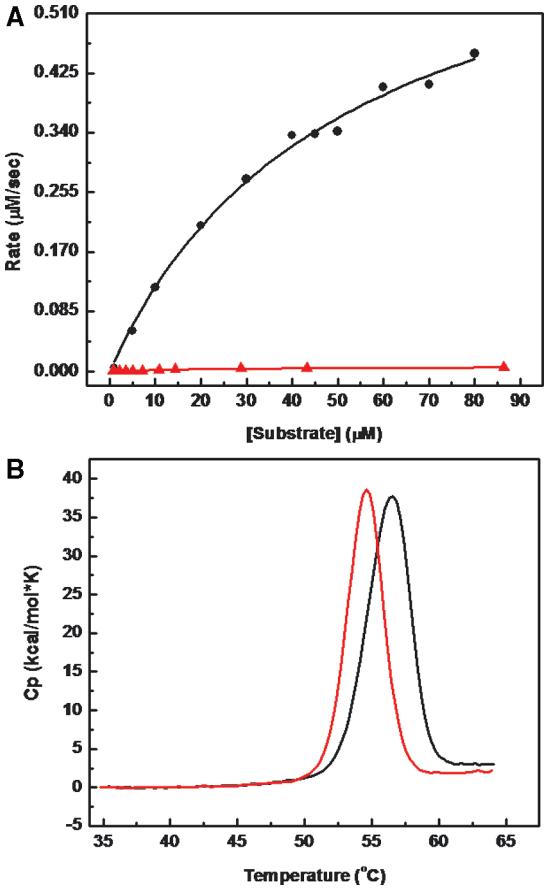

FIGURE 2: Enzymatic activities of wild-type SARS 3CL^{pro} vs the N28A mutant. (A) The enzymatic activities of wild-type 3CL^{pro} (●) and N28A (▲) were determined at 25 °C with an enzyme concentration of 1 μM in 10 mM sodium phosphate, 10 mM NaCl, 1 mM EDTA, and 1 mM TCEP (pH 7.4). The initial velocity (micromolar per second) is plotted as a function of substrate concentration. (B) Thermal denaturation of wild-type (black) and N28A (red) SARS 3CL^{pro} as determined by differential scanning calorimetry. Excess heat capacity is plotted as a function of temperature. Calorimetric scans for both proteins were performed at identical concentrations (0.2 mg/mL) at a scanning rate of 1 °C/min.

Asn28 Is Important for the Dimerization of 3CL^{pro}. The effect of the mutation on the oligomeric state of SARS 3CL^{pro} was evaluated using sedimentation velocity and sedimentation equilibrium ultracentrifugation. The data were analyzed using SEDFIT (*30*) and SEDPHAT (*32*), and all experimental sedimentation coefficient values were converted to $S_{20,w}$ in SEDPHAT. A sedimentation velocity profile of N28A at 20 °C, 50000 rpm, and a concentration of 0.5 mg/mL is shown in Figure 3A−C. Two peaks are observed in the continuous sedimentation distribution profile. The first peak is centered at 2.8 S and the second at 3.8 S, corresponding to the monomeric and dimeric species, respectively. These peaks are slightly shifted from their positions in the sedimentation profile for the wild-type enzyme which are at 2.6 and 4.1 S, respectively (shown in Figure 3D). In addition, the peaks are not well-separated, which may indicate that the kinetic rate constant for self-association in the mutant may differ from that of the wild-type enzyme, which sediments in two well-separated peaks. Although Asn28 is far from the dimerization interface, mutation of this residue to alanine has a detrimental effect on the ability of the protease to dimerize, although the effect does not appear to be as drastic as that previously observed with the S147A mutant which predominantly exists as a monomer in solution (*21*).

Sedimentation equilibrium ultracentrifugation was performed with the N28A mutant at three protein concentrations (0.25, 0.5, and 1 mg/mL) and three rotor speeds (15000, 20000, and 25000 rpm) at 20 °C for the evaluation of the dissociation constant for the mutant. The data were globally analyzed using the monomer−dimer self-association model in SEDPHAT (*32*). Panels E and F of Figure 3 show the results of the wild-type and N28A data sets at 0.5 mg/mL. The residuals are well-dispersed and fit well to the monomer−dimer model. The K_d obtained was 25.0 ± 5.1 μM, which is a 19.2-fold decrease compared to that of the wild-type enzyme which we determined to have a K_d of 1.3 μM under the same conditions (*21*).

Crystallographic Structure of N28A SARS 3CL^{pro}. The results obtained from the kinetic and ultracentrifugation experiments indicate that Asn28 is important for the activity and oligomeric state of SARS 3CL^{pro}. To investigate the structural basis for the low activity and the decrease in the level of dimerization observed with this mutant, the crystallographic structure of N28A 3CL^{pro} was determined at 2.35 Å resolution (*13*). The best crystals grew in hanging drop experiments with a 500 μL reservoir solution containing 1.0 M sodium malonate (pH 7.0) and 5−6% 2-propanol. Drops were made using 2 μL of reservoir solution and 2 μL of protein solution (6 mg/mL).

Table 2: Summary of Kinetics, Structural Stability, and Dimerization Data

protein	K_m (μM)[a]	k_{cat} (s^{-1})[a]	k_{cat}/K_m[a] (mM^{-1} s^{-1})	T_m (°C)[b]	ΔT_m[b] (°C)	K_d (μM)[c]
WT	56 ± 9	0.64 ± 0.05	11.4	56.50 ± 0.03	0	1.3 ± 0.8
N28A	68 ± 7	0.012 ± 0.001	0.176	54.75 ± 0.02	−1.75	25 ± 5

[a]Kinetic values were obtained by a global nonlinear least-squares fit of initial rate measurements at increasing substrate concentrations at an enzyme concentration of 1 μM. [b]Structural stability values were obtained by fitting excess heat capacity vs temperature data using software from this laboratory. [c]Dimerization K_d values were calculated from the global analysis of sedimentation equilibrium data at concentrations of 0.25 mg/mL (7.4 μM), 0.5 mg/mL (14.8 μM), and 1 mg/mL (29.5 μM) for each protein using the monomer−dimer self-association model using SEDPHAT (*32*).

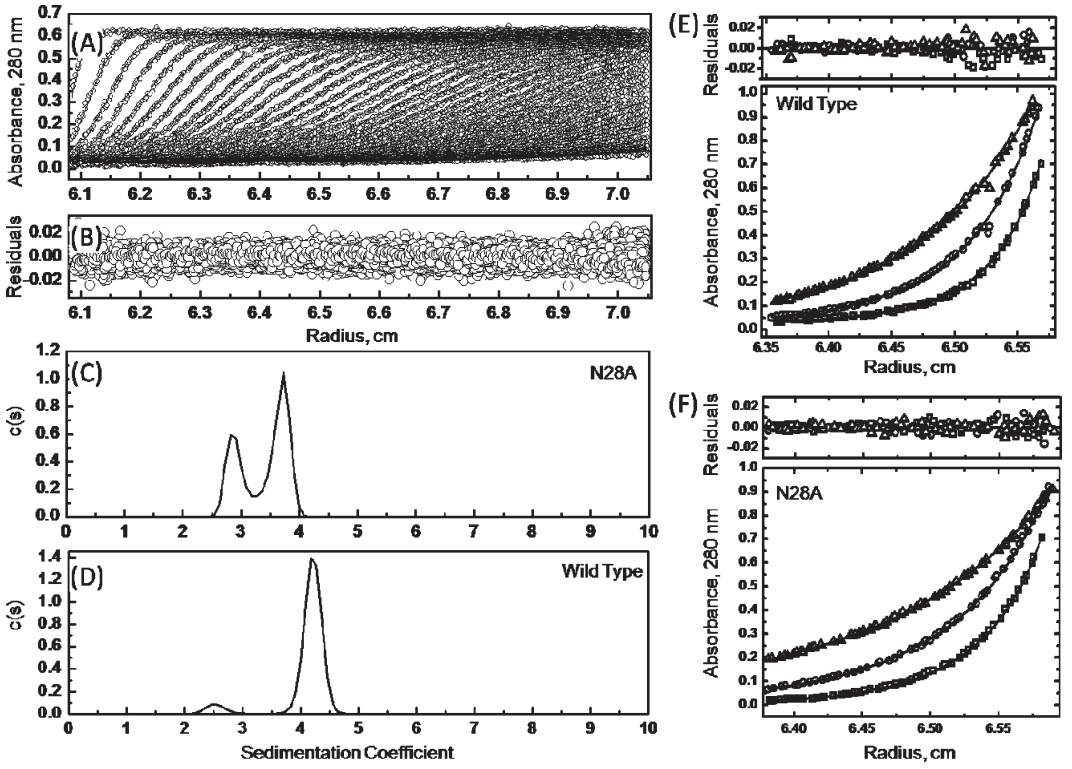

FIGURE 3: Sedimentation velocity and sedimentation equilibrium ultracentrifugation of N28A at 0.5 mg/mL. (A) Sedimentation velocity absorbance trace of N28A SARS 3CL^{pro} at 280 nm. The sedimentation of the N28A mutant was conducted with a Beckman Coulter XL-I analytical ultracentrifuge at 20 °C and 50000 rpm. (B) Residuals of the experimental fit of N28A SARS 3CL^{pro} at 0.5 mg/mL (14.8 μM). Continuous sedimentation coefficient distributions at 0.5 mg/mL (C) N28A SARS 3CL^{pro} and (D) wild-type SARS 3CL^{pro}. Sedimentation equilibrium ultracentrifugation of (E) wild-type SARS 3CL^{pro} and (F) N28A SARS 3CL^{pro} at 0.5 mg/mL. Sedimentation equilibrium experiments with wild-type and mutant SARS 3CL^{pro} were conducted at 20 °C at concentrations of 0.25, 0.5, and 1 mg/mL in six-channel centerpieces and globally analyzed with SEDPHAT (*32*). Data at 0.5 mg/mL (14.8 μM) are shown for both the wild type and N28A. The bottom graph in each panel shows the raw data at 15000 (△), 20000 (○), and 25000 rpm (□) and the corresponding global fits displayed in a solid line. The top graphs in each panel show the residuals for the given fits.

Crystals grew within 1−3 days at room temperature as clusters which were then separated into individual crystals for the diffraction experiments.

The structure of N28A SARS 3CL^{pro} was determined by molecular replacement using wild-type SARS 3CL^{pro} [PDB entry 2BX4 (*18*)] as a search model. The final model, comprising residues 3−138 and 142−301, was refined to 2.35 Å resolution with an R value of 21.7% (R_{free} = 27.7%). The N28A mutation did not cause any large changes in the overall tertiary organization of SARS 3CL^{pro} as shown in Figure 4A. The N28A structure aligns well with that of the wild-type enzyme [PDB entry 2BX4 (*18*)], with an rmsd of 0.555 Å over 271 Cα atoms. Inspection of the catalytic domains in the region surrounding the N28A mutation revealed that significant structural changes occur in and around the active site. One of the most striking consequences of the N28A mutation is the formation of a novel disulfide bond between the catalytic Cys145 residue and the Cys117 residue as depicted in Figure 5. This disulfide bridge is absent in crystal structures of the wild-type enzyme obtained under identical conditions (see, for example, ref *13*). The side chains of both residues flip almost 180° from their positions in the wild-type protein to form the only disulfide bond found in the protein. The drastic loss in enzymatic activity measured for N28A in the kinetic experiments is likely due to the new orientation of the side chain of Cys145, which points away from the active site cavity which would be expected to hinder substrate catalysis. Some or all of the interactions made by the side chain of Asn28 observed in the wild-type protease (Figure 1B) appear to be essential for directing the side chain of Cys145 into the active site cavity and Cys117 in the opposite direction. In addition to the loss of hydrogen bonding interactions made by the side chain of Asn28, structural rearrangements due to the change in van der Waals volume due to the mutation to the smaller alanine residue may also contribute to this effect. The formation of this disulfide bridge appears to be related to the loss of enzyme activity as suggested by experiments (not shown) in which enzyme activity was observed to increase as the concentration of a reducing agent in solution was increased.

Residues on the catalytic loop containing Cys145 also show a number of structural changes with respect to the wild-type structure. The side chain of Ser147 shifts from the position in which it is typically found in the wild-type structure, so that it is no longer in position to interact with the main chain atoms of Ser144 and Cys117 in the N28A mutant, as shown in Figure 6. The oxyanion hole formed by the backbone amides of Ser144 and Gly143 is completely collapsed. Moreover, electron density for residues 139−141 was not visible in the $2F_o - F_c$ electron density map of the N28A mutant, indicating that this portion of the loop is likely disordered. Disorder in this loop is significant due to the fact that these residues are located at the dimer interface (Figure 4B), and a significant decrease in the level of dimerization for this mutant was observed in the ultracentrifugation experiments. In wild-type 3CL^{pro} structures, Phe140 stacks with Tyr126 of the same monomer, which in turn makes a hydrophobic interaction with the side chain of Met6 of the opposing monomer; mutation of Phe140 to alanine has been observed to completely

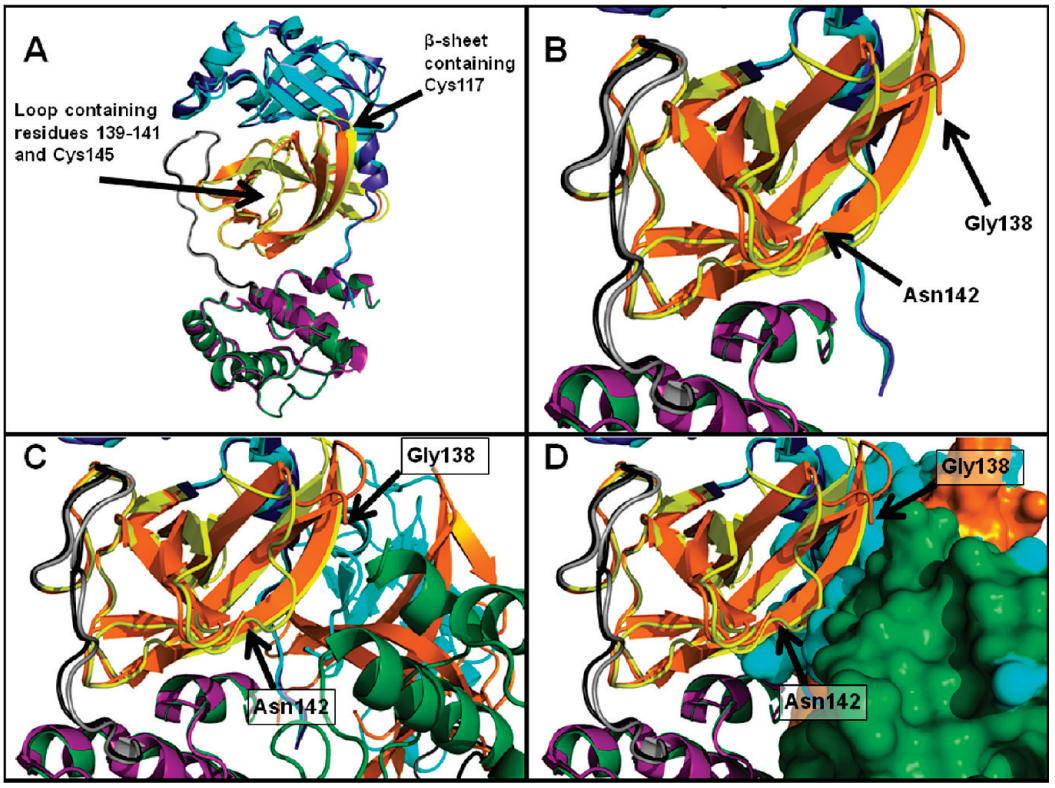

FIGURE 4: Alignment of the N28A and wild-type SARS 3CL^{pro} structures. (A) Structural alignment of wild-type SARS 3CL^{pro} [PDB entry 2BX4 (*18*)] and the N28A mutant (this work). Both proteins are depicted as monomers in ribbon representation and are colored by domain. Domain 1 (residues 3−100) is colored blue for wild-type 3CL^{pro} and cyan for N28A. Domain 2 (residues 101−183) is colored yellow for the wild type and orange for N28A. The loop region is colored gray for the wild type and black for N28A. Domain 3 (residues 201−301) is colored purple for the wild type and green for N28A. The rmsd for the alignment was 0.555 Å over 271 Cα atoms. The alignment was performed using Pymol, version 0.99 (*49*). (B) Close-up of the region surrounding residues 139−141 in the aligned wild-type and N28A SARS 3CL^{pro} structures shown in panel A. No electron density for these residues is observed for the N28A structure. Only one protomer of the dimer is shown for the sake of clarity. The aligned structures of wild-type SARS 3CL^{pro} and N28A 3CL^{pro} are shown in ribbon representation with the wild type and N28A mutant colored as in panel A. (C) Close-up of the same region shown in panel B, except depicting the entire N28A dimer in ribbon representation. Only the aligned monomer of wild-type 3CL^{pro} is shown for the sake of clarity. Colors of the subunits are the same as in panel A. (D) Close-up of the same region shown in panels B and C, with the other monomer of N28A depicted in surface representation. Domains colored as in panel A. In panels B−D, two arrows point to the locations of Gly138 and Asn142 in the N28A structure, which are the two residues flanking the region of the catalytic loop that is disordered in the N28A structure (residues 139−141).

disrupt the catalytic activity of the enzyme and reduces the level of dimerization to almost half that of the wild type (*26*). The side chain of Ser139 donates a hydrogen bond to the backbone carbonyl of Gly2 of the opposing chain. Previous studies performed with an S139A mutant showed a slightly diminished propensity for the enzyme to dimerize (*21*, *26*).

Additional residues located at the dimer interface were inspected for any structural rearrangements which could explain the decrease in the enzyme's propensity to dimerize. Figure 7 shows an overlay of the dimer interface of wild-type SARS 3CL^{pro} [PDB entry 2BX4 (*18*)] and the N28A mutant. The only major change observed in the positions of the first 14 residues of the N-terminus was a rotation in the side chain of Phe3. This residue has been mutated previously (*26*) and shown to have no effect on the oligomeric state of the enzyme, although the mutation did severely affect enzymatic activity. Similarly, only very small changes in the positions of the remaining residues at the interface are observed. While the possibility exists that the additive effect of these small changes results in the diminished capacity of the enzyme to dimerize, the most notable change observed is the lack of electron density for residues 139−141.

Since the only major structural change observed at the dimer interface of the N28A mutant is the disordering of the Ser139-Phe140-Leu141 loop, there is a strong possibility that the loss of the interactions made by one or all of these residues is linked to the decrease in the level of dimerization observed in the analytical ultracentrifugation experiments. Recently published crystallographic structures of SARS 3CL^{pro} monomeric mutants provide additional support for this possibility (*27*, *40*). Shi et al. (*27*) proposed the idea that the link between dimerization and catalysis in SARS 3CL^{pro} lies in an overlapping network of residues that are involved in both catalysis and dimerization and that a loss of the ability of the protease to dimerize leads to the trapping of key catalytic residues in a collapsed state, rendering the enzyme unable to efficiently perform catalysis. Specifically, the authors demonstrated that mutation of Arg298 (located at the C-terminus of the protein) resulted in a completely inactive and monomeric enzyme. In the wild type, Arg298 interacts with Met6 of the same chain, which in turn sits in a hydrophobic pocket with Phe140 and Tyr126 of the opposing chain. When the crystallographic structure of the monomeric R298A mutant was determined, a 40° rotation was observed between the catalytic domains and the third domain, despite the finding that all three domains retained their overall architecture. Inspection of the catalytic domains in the mutant reveals that a key catalytic loop has a changed conformation. In particular, residues Ser139, Phe140, and Leu141 switched from their standard loop conformation in the wild-type structure to form a short 3_{10}-helix in the

structure of the mutant. Moreover, a comparison of this structure to other known wild-type structures revealed that a similar 3_{10}-helix is present in wild-type structures with protomers in a catalytically inactive conformation and has also since been observed in the structure of another monomeric SARS 3CL^{pro} mutant (*40*).

The N28A crystallographic structure presented in this work provides additional support for the hypothesis that the region of

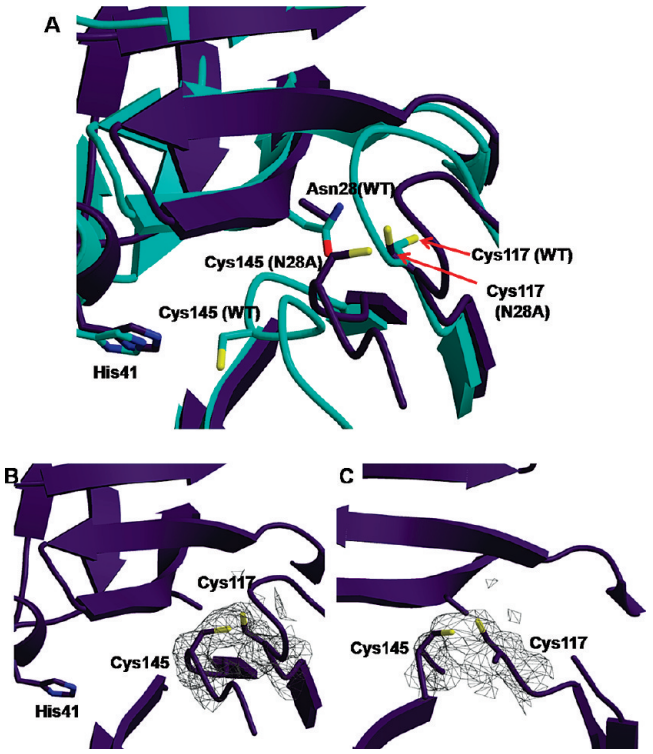

FIGURE 5: Disulfide bond formation between Cys145 and Cys117 in the N28A mutant. (A) Overlay of the active sites of the N28A mutant and wild-type SARS 3CL^{pro} showing the structural changes observed in residues Cys145 and Cys117 in the mutant protein. The proteins are shown in ribbon representation and colored teal (WT) and purple (N28A). Side chains are shown as sticks and colored by atom type with nitrogens colored blue, oxygens red, sulfurs yellow, and carbons teal and purple for the wild type and mutant, respectively. (B) The $2F_o - F_c$ electron density map of the N28A mutant showing the electron density between the catalytic residue Cys145 and Cys117 contoured to 1σ. Cys145 and Cys117 are colored by atom type with sulfurs colored yellow and carbons teal and purple for the wild type and mutant, respectively. (C) Different view of panel B showing the electron density between Cys145 and Cys117, indicating the existence of a disulfide bond.

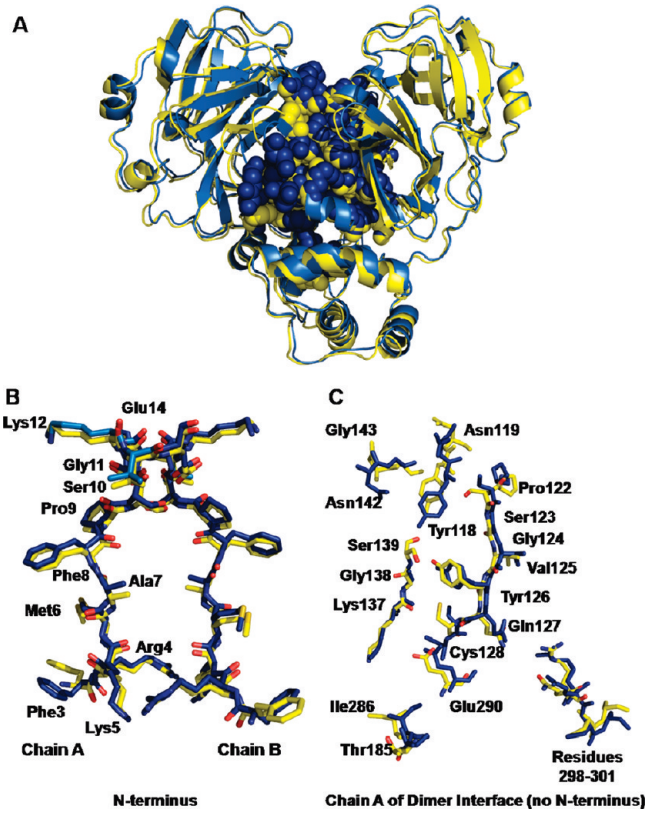

FIGURE 7: Comparison of the wild-type and N28A SARS 3CL^{pro} dimer interfaces. (A) Overlay of wild-type SARS 3CL^{pro} [PDB entry 2BX4 (*18*)] and N28A SARS 3CL^{pro}. The proteins are shown in ribbon representation and are colored yellow for the wild type and blue for the N28A mutant. Residues at the dimer interface are shown as spheres. (B) Overlay of the first 14 residues of the N-terminus of the proteins. Residues are shown in stick representation and are colored by atom type with nitrogens colored blue, oxygens red, sulfurs tan, and carbons dark blue or yellow for the wild type or N28A, respectively. (C) Chain A of residues at the dimer interface. Residues are displayed in stick representation and colored by atom type as in panel B. Residues involved in binding at the dimer interface were calculated with Ligplot (*50*).

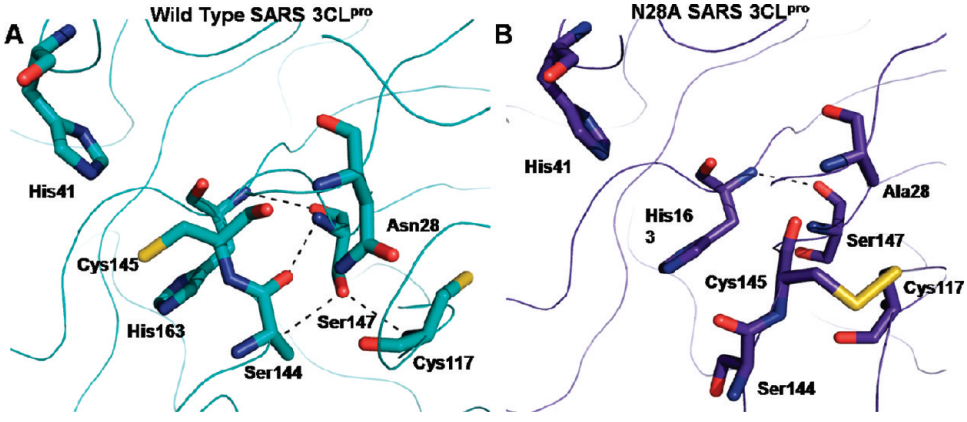

FIGURE 6: Ser147 interactions in the structures of wild-type SARS 3CL^{pro} and N28A SARS 3CL^{pro}. Hydrogen bonding interactions made by Ser147 within the active sites of (A) wild-type SARS 3CL^{pro} [PDB entry 2BX4 (*18*)] and (B) N28A SARS 3CL^{pro} [PDB entry 3FZD (this work)] are depicted with black dotted lines. Hydrogen bonding interactions were calculated using Chimera (*47*). Structures shown were aligned in PyMol (version 0.99) (*49*). The rmsd for the alignment was 0.555 Å over 271 Cα atoms.

the catalytic loop containing residues 139−141 may indeed be a part of an intricate overlapping network of interactions that is responsible for regulating both dimerization and catalysis in SARS 3CL^{pro}. Furthermore, the dual role of these residues in both dimerization and catalysis also explains how residues located in regions of the protein close to the active site cavity and away from the dimerization interface, such as Asn28 and Ser147, affect the oligomeric state of the protein. Perturbation of key interactions that affect the conformation of these key loop regions may largely affect the oligomeric state of the protein despite the fact that the residues involved are not located directly at the dimer interface.

The fundamental importance of long-range interactions in protein structure and function has been demonstrated in a wide variety of proteins (*21*, *41*−*46*). It has become increasingly clear that long-distance communication is not solely restricted to proteins falling into the category of traditional allosteric systems, but instead a common occurrence in many globular proteins. Long-range interactions regulate processes important for ligand binding, enzyme catalysis, protein folding, and oligomerization (*41*). For a number of these proteins, it has been shown that dynamic intramolecular networks exist that can be perturbed through the introduction of a single point mutation (*21*, *41*, *42*, *45*, *46*). Clarkson et al. showed that point mutations made to the serine protease inhibitor Eglin c altered the side chain dynamics of a contiguous series of residues as much as 13 Å from the point of mutation (*41*). Ornithine decarboxylase, a validated drug target for African sleeping sickness, has also displayed evidence of long-range energetic coupling between the active site of the enzyme (formed at the dimer interface) and individual residues located in distal regions of the interface (∼15−20 Å away) that play key roles in enzyme function without largely affecting dimer formation (*42*). The characterization of these integrated networks is essential to understanding major contributors to protein stability and function and can be advantageous to consider when performing structure-based drug design under conditions in which competitive inhibitors cannot be developed.

Conclusions. Asn28 is a conserved residue located adjacent to the active site of SARS 3CL^{pro}. Mutation of this residue to an alanine drastically reduced enzymatic activity and resulted in a 19.2-fold decrease in the dimerization K_d as measured by sedimentation equilibrium ultracentrifugation. Crystallographic analysis of the mutant revealed large changes within the active site cavity of the protein, specifically in the movement of the catalytic residue, Cys145, which moved from its original position in the wild-type enzyme to form a novel disulfide bond with the side chain of Cys117, which also made a large shift from its original position in the wild-type protein. This large change is likely the cause for the decrease observed in the k_{cat} value of the mutant protein with respect to that of the wild-type enzyme. Residues 139−141 were disordered in the crystal structure and were the only residues at the dimer interface of the protein to display largely significant changes, indicating that the change in conformation of these residues may be the cause of the 19.2-fold decrease in the dimerization K_d. These results support our recent finding that dimerization of SARS 3CL^{pro} is regulated through long-range cooperative interactions and that dimerization and catalysis are linked through key residues that maintain the structural integrity of the enzyme.

ACKNOWLEDGMENT

Beamline X6a of the National Synchrotron Light Source funded by the National Institute of General Medical Service is gratefully acknowledged.

REFERENCES

1. Drosten, C., Gunther, S., Preiser, W., van der Werf, S., Brodt, H.-R., Becker, S., Rabenau, H., Panning, M., Kolesnikova, L., Fouchier, R. A. M., Berger, A., Burguiere, A.-M., Cinatl, J., Eickmann, M., Escriou, N., Grywna, K., Kramme, S., Manuguerra, J.-C., Muller, S., Rickerts, V., Sturmer, M., Vieth, S., Klenk, H.-D., Osterhaus, A. D. M. E., Schmitz, H., and Doerr, H. W. (2003) Identification of a Novel Coronavirus in Patients with Severe Acute Respiratory Syndrome. *N. Engl. J. Med. 348*, 1967–1976.
2. Guan, Y., Zheng, B. J., He, Y. Q., Liu, X. L., Zhuang, Z. X., Cheung, C. L., Luo, S. W., Li, P. H., Zhang, L. J., Guan, Y. J., Butt, K. M., Wong, K. L., Chan, K. W., Lim, W., Shortridge, K. F., Yuen, K. Y., Peiris, J. S. M., and Poon, L. L. M. (2003) Isolation and Characterization of Viruses Related to the SARS Coronavirus from Animals in Southern China. *Science 302*, 276–278.
3. Kuiken, T., Fouchier, R. A., Schutten, M., Rimmelzwaan, G. F., van Amerongen, G., van Riel, D., Laman, J. D., de Jong, T., van Doornum, G., and Lim, W. (2003) Newly discovered coronavirus as the primary cause of severe acute respiratory syndrome. *Lancet 362*, 263–270.
4. Peiris, J., Lai, S., Poon, L., Guan, Y., Yam, L., Lim, W., Nicholls, J., Yee, W., Yan, W., and Cheung, M. (2003) Coronavirus as a possible cause of severe acute respiratory syndrome. *Lancet 361*, 1319–1325.
5. van der Hoek, L., Pyrc, K., and Berkhout, B. (2006) Human coronavirus NL63, a new respiratory virus. *FEMS Microbiol. Rev. 30*, 760–773.
6. Woo, P. C. Y., Lau, S. K. P., Chu, C.-m., Chan, K.-h., Tsoi, H.-w., Huang, Y., Wong, B. H. L., Poon, R. W. S., Cai, J. J., Luk, W.-k., Poon, L. L. M., Wong, S. S. Y., Guan, Y., Peiris, J. S. M., and Yuen, K.-y. (2005) Characterization and Complete Genome Sequence of a Novel Coronavirus, Coronavirus HKU1, from Patients with Pneumonia. *J. Virol. 79*, 884–895.
7. Thiel, V., Ivanov, K. A., Putics, A., Hertzig, T., Schelle, B., Bayer, S., Weissbrich, B., Snijder, E. J., Rabenau, H., Doerr, H. W., Gorbalenya, A. E., and Ziebuhr, J. (2003) Mechanisms and enzymes involved in SARS coronavirus genome expression. *J. Gen. Virol. 84*, 2305–2315.
8. Ziebuhr, J., Snijder, E. J., and Gorbalenya, A. E. (2000) Virus-encoded proteinases and proteolytic processing in the Nidovirales. *J. Gen. Virol. 81*, 853–879.
9. Wei, P., Fan, K., Chen, H., Ma, L., Huang, C., Tan, L., Xi, D., Li, C., Liu, Y., Cao, A., and Lai, L. (2006) The N-terminal octapeptide acts as a dimerization inhibitor of SARS coronavirus 3C-like proteinase. *Biochem. Biophys. Res. Commun. 339*, 865–872.
10. Chou, C.-Y., Chang, H.-C., Hsu, W.-C., Lin, T.-Z., Lin, C.-H., and Chang, G.-G. (2004) Quaternary Structure of the Severe Acute Respiratory Syndrome (SARS) Coronavirus Main Protease. *Biochemistry 43*, 14958–14970.
11. Chen, S., Chen, L., Tan, J., Chen, J., Du, L., Sun, T., Shen, J., Chen, K., Jiang, H., and Shen, X. (2005) Severe Acute Respiratory Syndrome Coronavirus 3C-like Proteinase N Terminus Is Indispensable for Proteolytic Activity but Not for Enzyme Dimerization: Biochemical and Thermodynamic Investigation in Conjunction with Molecular Dynamics Simulations. *J. Biol. Chem. 280*, 164–173.
12. Ding, L., Zhang, X.-X., Wei, P., Fan, K., and Lai, L. (2005) The interaction between severe acute respiratory syndrome coronavirus 3C-like proteinase and a dimeric inhibitor by capillary electrophoresis. *Anal. Biochem. 343*, 159–165.
13. Hsu, M.-F., Kuo, C.-J., Chang, K.-T., Chang, H.-C., Chou, C.-C., Ko, T.-P., Shr, H.-L., Chang, G.-G., Wang, A. H.-J., and Liang, P.-H. (2005) Mechanism of the Maturation Process of SARS-CoV 3CL Protease. *J. Biol. Chem. 280*, 31257–31266.
14. Shi, J., Wei, Z., and Song, J. (2004) Dissection Study on the Severe Acute Respiratory Syndrome 3C-like Protease Reveals the Critical Role of the Extra Domain in Dimerization of the Enzyme: Defining the Extra Domain as a New Target for Design of Highly Specific Protease Inhibitors. *J. Biol. Chem. 279*, 24765–24773.
15. Shi, J., and Song, J. (2006) The catalysis of the SARS 3C-like protease is under extensive regulation by its extra domain. *FEBS J. 273*, 1035–1045.
16. Kuo, C.-J., Chi, Y.-H., Hsu, J. T.-A., and Liang, P.-H. (2004) Characterization of SARS main protease and inhibitor assay using a fluorogenic substrate. *Biochem. Biophys. Res. Commun. 318*, 862–867.
17. Fan, K., Wei, P., Feng, Q., Chen, S., Huang, C., Ma, L., Lai, B., Pei, J., Liu, Y., Chen, J., and Lai, L. (2004) Biosynthesis, Purification, and Substrate Specificity of Severe Acute Respiratory Syndrome Coronavirus 3C-like Proteinase. *J. Biol. Chem. 279*, 1637–1642.

18. Tan, J., Verschueren, K. H. G., Anand, K., Shen, J., Yang, M., Xu, Y., Rao, Z., Bigalke, J., Heisen, B., and Mesters, J. R. (2005) pH-dependent Conformational Flexibility of the SARS-CoV Main Proteinase (Mpro) Dimer: Molecular Dynamics Simulations and Multiple X-ray Structure Analyses. *J. Mol. Biol. 354*, 25–40.
19. Hsu, W.-C., Chang, H.-C., Chou, C.-Y., Tsai, P.-J., Lin, P.-I., and Chang, G.-G. (2005) Critical Assessment of Important Regions in the Subunit Association and Catalytic Action of the Severe Acute Respiratory Syndrome Coronavirus Main Protease. *J. Biol. Chem. 280*, 22741–22748.
20. Lai, L., Han, X., Chen, H., Wei, P., Huang, C., Liu, S., Fan, K., Zhou, L., Liu, Z., Pei, J., and Liu, Y. (2006) Quaternary Structure, Substrate Selectivity and Inhibitor Design for SARS 3C-Like Proteinase. *Curr. Pharm. Des. 12*, 4555–4564.
21. Barrila, J., Bacha, U., and Freire, E. (2006) Long-Range Cooperative Interactions Modulate Dimerization in SARS 3CLpro. *Biochemistry 45*, 14908–14916.
22. Graziano, V., McGrath, W. J., Yang, L., and Mangel, W. F. (2006) SARS CoV Main Proteinase: The Monomer-Dimer Equilibrium Dissociation Constant. *Biochemistry 45*, 14632–14641.
23. Chen, H., Wei, P., Huang, C., Tan, L., Liu, Y., and Lai, L. (2006) Only One Protomer Is Active in the Dimer of SARS 3C-like Proteinase. *J. Biol. Chem. 281*, 13894–13898.
24. Graziano, V., McGrath, W. J., DeGruccio, A. M., Dunn, J. J., and Mangel, W. F. (2006) Enzymatic activity of the SARS coronavirus main proteinase dimer. *FEBS Lett. 580*, 2577–2583.
25. Yang, H., Yang, M., Ding, Y., Liu, Y., Lou, Z., Zhou, Z., Sun, L., Mo, L., Ye, S., Pang, H., Gao, G. F., Anand, K., Bartlam, M., Hilgenfeld, R., and Rao, Z. (2003) The crystal structures of severe acute respiratory syndrome virus main protease and its complex with an inhibitor. *Proc. Natl. Acad. Sci. U.S.A. 100*, 13190–13195.
26. Chen, S., Zhang, J., Hu, T., Chen, K., Jiang, H., and Shen, X. (2008) Residues on the Dimer Interface of SARS Coronavirus 3C-like Protease: Dimer Stability Characterization and Enzyme Catalytic Activity Analysis. *J. Biochem. 143*, 525–536.
27. Shi, J., Sivaraman, J., and Song, J. (2008) Mechanism for Controlling Dimer-monomer Switch and Coupling Dimerization to Catalysis of the SARS-CoV 3C-Like Protease. *J. Virol. 82*, 4620–4629.
28. Zhong, N., Zhang, S., Zou, P., Chen, J., Kang, X., Li, Z., Liang, C., Jin, C., and Xia, B. (2008) Without its N-Finger, SARS-CoV Main Protease can Form a Novel Dimer through its C-Terminal Domain. *J. Virol. 82*, 4227–4234.
29. Bacha, U., Barrila, J., Velazquez-Campoy, A., Leavitt, S. A., and Freire, E. (2004) Identification of Novel Inhibitors of the SARS Coronavirus Main Protease $3CL^{pro}$. *Biochemistry 43*, 4906–4912.
30. Schuck, P. (2000) Size-Distribution Analysis of Macromolecules by Sedimentation Velocity Ultracentrifugation and Lamm Equation Modeling. *Biophys. J. 78*, 1606–1619.
31. Schuck, P. (2003) On the analysis of protein self-association by sedimentation velocity analytical ultracentrifugation. *Anal. Biochem. 320*, 104–124.
32. Vistica, J., Dam, J., Balbo, A., Yikilmaz, E., Mariuzza, R. A., Rouault, T. A., and Schuck, P. (2004) Sedimentation equilibrium analysis of protein interactions with global implicit mass conservation constraints and systematic noise decomposition. *Anal. Biochem. 326*, 234–256.
33. Navaza, J. (1994) AMoRe: An automated package for molecular replacement. *Acta Crystallogr. A50*, 157–163.
34. Otwinowski, Z., and Minor, W. (1997) Processing of X-ray diffraction data collected in oscillation mode. *Methods Enzymol. 277*, 307–326.
35. Collaborative Computational Project Number 4 (1994) The CCP4 Suite: Programs for Protein Crystallography. *Acta Crystallogr. D50*, 760–763.
36. Jones, T., Zou, J., Cowan, S., and Kjelgaard, M. (1991) Improved methods for binding protein models to electron density maps and the location of errors in these models. *Acta Crystallogr. A42*, 110–119.
37. Perrakis, A., Harkiolaki, M., Wilson, K., and Lamzin, V. (2001) ARP/wARP and molecular replacement. *Acta Crystallogr. D57*, 1445–1450.
38. Laskowski, R., MacArthur, M., Moss, D., and Thornton, J. (1993) PROCHECK: A program to check the sterochemical quality of protein structures. *J. Appl. Crystallogr. 26*, 283–291.
39. Bacha, U., Barrila, J., Gabelli, S. B., Kiso, Y., Mario Amzel, L., and Freire, E. (2008) Development of Broad-Spectrum Halomethyl Ketone Inhibitors Against Coronavirus Main Protease 3CLpro. *Chem. Biol. Drug Des. 72*, 34–49.
40. Chen, S., Hu, T., Zhang, J., Chen, J., Chen, K., Ding, J., Jiang, H., and Shen, X. (2008) Mutation of Gly-11 on the Dimer Interface Results in the Complete Crystallographic Dimer Dissociation of Severe Acute Respiratory Syndrome Coronavirus 3C-like Protease: Crystal Structure with Molecular Dynamics Simulations. *J. Biol. Chem. 283*, 554–564.
41. Clarkson, M. W., and Lee, A. L. (2004) Long-range dynamic effects of point mutations propagate through side chains in the serine protease inhibitor eglin c. *Biochemistry 43*, 12448–12458.
42. Myers, D. P., Jackson, L. K., Ipe, V. G., Murphy, G. E., and Phillips, M. A. (2001) Long-range interactions in the dimer interface of ornithine decarboxylase are important for enzyme function. *Biochemistry 40*, 13230–13236.
43. Ohtaka, H., Schon, A., and Freire, E. (2003) Multidrug resistance to HIV-1 protease inhibition requires cooperative coupling between distal mutations. *Biochemistry 42*, 13659–13666.
44. Perez-Jimenez, R., Godoy-Ruiz, R., Parody-Morreale, A., Ibarra-Molero, B., and Sanchez-Ruiz, J. M. (2006) A simple tool to explore the distance distribution of correlated mutations in proteins. *Biophys. Chem. 119*, 240–246.
45. Rajagopalan, P. T., Lutz, S., and Benkovic, S. J. (2002) Coupling interactions of distal residues enhance dihydrofolate reductase catalysis: Mutational effects on hydride transfer rates. *Biochemistry 41*, 12618–12628.
46. Spudich, G., Lorenz, S., and Marqusee, S. (2002) Propagation of a single destabilizing mutation throughout the *Escherichia coli* ribonuclease HI native state. *Protein Sci. 11*, 522–528.
47. Pettersen, E. F., Goddard, T. D., Huang, C. C., Couch, G. S., Greenblatt, D. M., Meng, E. C., and Ferrin, T. E. (2004) UCSF Chimera: A Visualization System for Exploratory Research and Analysis. *J. Comput. Chem. 25*, 1605–1612.
48. Thompson, J. D., Higgins, D. G., and Gibson, T. J. (1994) CLUSTAL W: Improving the sensitivity of progressive multiple sequence alignment through sequence weighting, position-specific gap penalties and weight matrix choice. *Nucleic Acids Res. 22*, 4673–4680.
49. DeLano, W. (2007) The PyMOL Molecular Graphics System, 0.99 ed., DeLano Scientific LLC, San Carlos, CA.
50. Wallace, A. C., Laskowski, R. A., and Thornton, J. M. (1995) LIGPLOT: A program to generate schematic diagrams of protein-ligand interactions. *Protein Eng. 8*, 127–134.